

Review



Distributed fiber optic strain sensing for crack detection with Brillouin shift spectrum back analysis

Structural Health Monitoring
I–14
© The Author(s) 2023
Article reuse guidelines:
sagepub.com/journals-permissions
DOI: 10.1177/14759217231206857
journals.sagepub.com/home/shm

Ruonan Ou¹, Linqing Luo² and Kenichi Soga¹

Abstract

Material cracking is one of the key mechanisms contributing to structural failure. Distributed fiber optic sensing (DFOS) can measure the strain profile along optical fiber distributively. However, the conventional strain measurement using a Brillouin-DFOS system (Brillouin optical time-domain analysis/reflectometry (BOTDA/R)) has a decimeter-order spatial resolution, making it difficult to measure the highly localized strain generated by a sub-millimeter crack. This paper introduces a crack analysis method based on decomposing the Brillouin scattering spectrum to overcome the spatial resolution induced crack measurement limitation of the BOTDA/R system. The method uses the non-negative least squares algorithm to back-calculate the strain profile within the spatial resolution around each measurement point. The performance of this method is verified by a four point bending test of a brittle slag cement-cement-bentonite beam. The crack width estimation error is improved to ±0.005 mm for a crack as narrow as 0.76 mm.

Keywords

Distributed fiber optic sensing, Brillouin scattering, strain sensing, structural health monitoring, crack detection

Introduction

Detecting the development of cracks in a structure is a crucial part of structural health monitoring (SHM) in the context of safety evaluation as they affect the integrity and service life of the structure. 1-4 It is important to conduct effective crack monitoring because the crack detection helps reduce the risk of structural failure. A variety of monitoring techniques have been proposed and adopted to detect crack development in a structure, including acoustic emission, infrared thermography, ground-penetrating radar, fiber Bragg grating, digital image correlation, computer vision, and so on. As the timing and position of crack openings are usually unforeseen, a solution that has wide coverage and allows continuous monitoring is attractive.

Distributed fiber optic sensing (DFOS) stands out as a prominent technology with the capability to detect cracks across extensive areas. Within the array of DFOS technologies, optical frequency domain reflectometry (OFDR) garners attention due to its submillimeter spatial resolution. Various crack detection methodologies have been pioneered to enhance both the identification and localization of cracks using OFDR. 11–14 Nonetheless, its inherent limitation lies in its sensing range, typically confined between 50 and

100 m, which restricts its applicability in expansive infrastructural settings.

Another DFOS technique, Brillouin scattering-based DFOS (Brillouin-DFOS) technology has become one of the most widely used technologies in the field of SHM.¹⁵ There are two primary classifications under this banner: Brillouin optical time-domain analysis (BOTDA) and Brillouin optical time-domain reflectometry (BOTDR). These tools are prized for their kilometer-order sensing distances combined with decimeter-order sampling intervals, making them invaluable for monitoring expansive structures. A pressing concern, however, is their spatial resolution, typically restrained between 0.5 and 1.0 m. This limitation becomes palpable when monitoring millimeter-order cracks: such a crack, when subjected to significant strain, will manifest over an extended length

Corresponding author:

Linqing Luo, Earth and Environmental Sciences Area, Lawrence Berkeley National Laboratory, #I Cyclotron Road, MS 74R316C, Berkeley, CA 94720, USA.

Email:linqingluo@lbl.gov

¹Department of Civil and Environment Engineering, University of California, Berkeley, CA, USA

²Earth and Environmental Sciences Area, Lawrence Berkeley National Laboratory, Berkeley, CA, USA

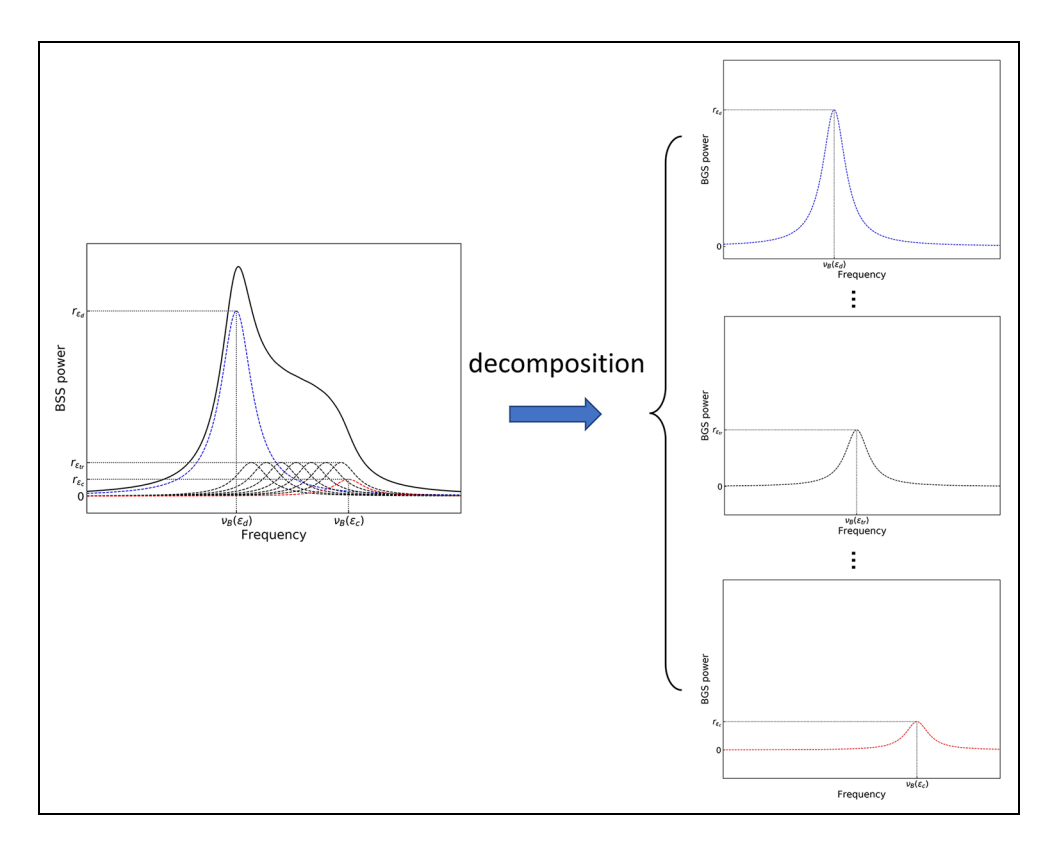


Figure 1. Conceptual overview.

of about 0.5–1 m in the BOTDA/R system due to its spatial resolution. As a consequence, the actual intensity and scope of the strain are notably misjudged this delineates the spatial resolution induced measurement challenge in the prevailing BOTDA/R systems.

Addressing this conundrum, researchers have proposed three predominant strategies: (1) refining the interrogator system to achieve sub-10-cm spatial resolutions, albeit at the expense of truncating the sensing range to 500 m^{1,16–18}; (2) optimizing fiber installation techniques, exemplified by Ravet et al.'s suggestion to use the SMARTape which fosters initial delamination between the fiber and the sensing target, thus permitting crack detection even with 1 m spatial resolution interrogators. 19 It's crucial to underscore that while this method is apt for surface attachments, the predominant demand lies in embedding the fibers within the structure; (3) reverse engineering the strain profile by juxtaposing the recorded strain profile against the Brillouin scattering spectrum (BSS) especially for pronounced tensile strain detection.²⁰

In this study, we delve into an advanced methodology tailored to unveil the intricate data encompassed in the BSS. While most BOTDA/R systems provide the BSS for every sampling point, capturing a holistic view of the

strain within the spatial resolution,²¹ conventional methods primarily focus on extracting information from the peak frequency data for crack detection. Contrasting this norm, our novel approach hinges on a comprehensive BSS-based analysis. This methodology is adept at pinpointing crack-specific information, all the while retaining the essential attribute of expansive sensing ranges. Instead of restricting the examination to the spectrum indicative of maximal tensile strain, our algorithm holistically interprets the entire BSS components, as illustrated by the red, blue, and black dashed lines in Figure 1.

To provide clarity on our innovation, we introduce a least squares-driven BSS decomposition algorithm in this manuscript. Preliminary evaluations, built on a data set from a beam crack test, attest to its robustness: it elevates the resolution accuracy of the estimated strain profile to an impressive 1.3 mm, with an exceptionally minor error deviation of approximately 0.005 mm, even for a crack as subtle as 0.76 mm with an assumption of the presence of a singular crack within each spatial resolution window (SRW). Our research doesn't merely bridge the prevailing limitations in BOTDA/R system's spatial resolution; it illuminates a pioneering path in maximizing the utility of the BSS in the domain of SHM.

BSS in matrix format

Consider a scenario where we have n distinct strain values $(\varepsilon_i$, where i=1,...,n) distributed along a length l_{ε_i} within a spatial resolution L (given as $L = \sum_{i=1}^{n} l_{\varepsilon_i}$) around a measurement point located at Z. The BSS can then be expressed as:

$$G(\nu) = \sum_{i=1}^{n} r_{\varepsilon_i} g(\nu, \nu_B(\varepsilon_i))$$
 (1)

where r_{ε_i} (defined as $r_{\varepsilon_i} = l_{\varepsilon_i}/L$) represents the spatial resolution ratio for the section of length l_{ε_i} corresponding to strain value ε_i relative to the overall spatial resolution L. The term $g(\nu, \nu_B(\varepsilon_i))$ denotes the spontaneous Brillouin scattering under strain ε_i . Consequently, the measured BSS, denoted as $G(\nu)$, can be conceptualized as the result of an inner product involving two matrices:

$$G = SR \tag{2}$$

In this equation, BSS represents the measured BSS. Specifically, G forms a column vector (of size m) comprising BSS power data at various frequencies collected by the BOTDA/R system at discrete sampling points along the fiber. The frequencies, $\nu_1, \nu_2, ..., \nu_m$, correspond to the BSS frequencies determined by the interrogator frequency scanning step or frequency resolution within the Fast Fourier Transform.

Matrix S (of size $m \times n$) is composed of the BSS data associated with the n distinct strain values $(\varepsilon_1, \varepsilon_2, ... \varepsilon_n)$ encountered within the SRW of the sampling point. Vector R is also a column vector (of size n), with its elements corresponding to the spatial ratios of the n strain values $(\varepsilon_1, \varepsilon_2, ... \varepsilon_n)$.

To deduce the strain profile from the BSS data, $[\varepsilon_1, \varepsilon_2, ... \varepsilon_n]$ and their corresponding spatial ratios $[r_{\varepsilon_1}, r_{\varepsilon_2}, ..., r_{\varepsilon_n}]$ must be determined from Equation (2) given a known G. However, solving this equation is challenging due to two main reasons:

- (1) both *S* and *R* are unknown;
- (2) $g(\nu_i, \nu_B(\varepsilon_i))$ represents a nonlinear function of ε_i .

To address these challenges, Equation (2) must be transformed into a linear equation involving the unknowns. The first step involves reducing the number of unknowns. While $\varepsilon_1, \varepsilon_2, ... \varepsilon_n$ are indeed unknown, their range (defined as the maximum and minimum strain estimation $[a_{\min}, a_{\max}]$) can be estimated based on the structural deformation mechanism. Given that the maximum strain the optical fiber can withstand is approximately $10,000~\mu\varepsilon$, we can set a_{\max} as $10,000~\mu\varepsilon$. The research objective here is to estimate tensile strain due to cracking. Hence, a_{\min} can be conservatively estimated as slightly less than $0~\mu\varepsilon$ (e.g., $-1000~\mu\varepsilon$) to encompass the crack initiation phase and account for minimal potential compression.

With this context in mind, we introduce a new vector, C, which represents strain values within the range between the maximum and minimum strain. C is defined as $[c_1, c_2, ...c_p]$, where c_i values are uniformly distributed within $[a_{\min}, a_{\max}]$. Specifically, $c_i = a_{\min} + \frac{a_{\max} - a_{\min}}{p-1}$ (i-1), where $\frac{a_{\max} - a_{\min}}{p-1}$ represents the strain resolution within this analysis method.

By assuming that all the strain values c_i happen within the SRW, matrix S in Equation (2) is expanded as matrix S_L in Equations (4) and (5). The spatial ratio of c_i over the spatial resolution L, $(=l_{c_i}/L)$, is defined as r_{c_i} . The r_{c_i} s form the vector R_L in the two equations below. In this case, the problem of solving $[\varepsilon_1, \varepsilon_2, ... \varepsilon_n]$ and $[r_{\varepsilon_1}, r_{\varepsilon_2}, ..., r_{\varepsilon_n}]$ in Equation (2) is converted to solving $[r_{c_1}, r_{c_2}, ..., r_{c_p}]$ in Equation (4) with known G and known S_L .

Instead of only considering the strain values that do occur, all the possible strain values are initially assumed to happen. The final solution to Equation (4) will reveal which strain values do occur and which do not. By definition, r_{c_i} s need to be within [0,1] and their sum must be $1\left(\sum_{i=1}^{p} r_{c_i} = 1\right)$. The strain value (c_i) corresponding to the spatial ratio (r_{c_i}) that is solved to be zero does not occur. If r_{c_i} is solved to be positive, its corresponding c_i occurs and occupies the length of $r_{c_i}L$ within the SRW.

$$G = S_{L}R_{L}$$

$$G = \begin{bmatrix} G(\nu_{1}) \\ G(\nu_{2}) \\ \dots \\ G(\nu_{m}) \end{bmatrix}$$

$$S_{L} = \begin{bmatrix} g(\nu_{1}, \nu_{B}(c_{1})) & g(\nu_{1}, \nu_{B}(c_{2})) & \dots & g(\nu_{1}, \nu_{B}(c_{p})) \\ g(\nu_{2}, \nu_{B}(c_{1})) & g(\nu_{2}, \nu_{B}(c_{2})) & \dots & g(\nu_{2}, \nu_{B}(c_{p})) \\ \dots & \dots & \dots & \dots \\ g(\nu_{m}, \nu_{B}(c_{1})) & g(\nu_{m}, \nu_{B}(c_{2})) & \dots & g(\nu_{m}, \nu_{B}(c_{p})) \end{bmatrix}$$

$$R_{L} = \begin{bmatrix} r_{c_{1}} \\ r_{c_{2}} \\ \dots \\ r_{c_{p}} \end{bmatrix}$$

$$(5)$$

Least squares-based linear equation system solving method

Non-negative least squares (NNLS) algorithm is proposed to solve Equation (4). The problem is transformed to an optimization problem with constraints in the form of Equation (6) to Equation (9). The goal is to find the values of r_{ci} that minimizes the squared error function $||S_L R_L - G||^2$ with the constraints of r_{ci} in the range of [0, 1], and the sum of the r_{ci} values equals 1.

$$\operatorname{argmin}_{R_L} \parallel S_L R_L - G \parallel^2, \tag{6}$$

subject to

$$0 \leq r_{c_i} \geq 1, i = 1, ..., p \tag{7}$$

$$\sum_{i=1}^{p} c_i = 1, i = 1, ..., p$$
 (8)

Because Equation (6) is equivalent to Equation (9), the goal is to find the optimum point of a convex quadratic function of R_L . The method used to solve this problem is the active-set method, 22 where the active set is defined as the set of active constraints. The *i*th constraint is active if the solution of r_{c_i} can be negative when assuming no constraints. The method initially considers all constraints as active constraints and the estimation of r_{c_i} values starts from 0. After each iteration, the values of r_{c_i} are modified and the constraints are removed from the active set so the cost function becomes smaller and smaller. 23

$$\operatorname{argmin}_{R_L} \left(\frac{1}{2} R_L^T S_L^T S_L R_L - y^T S_L R_L \right) \tag{9}$$

Experiment

The algorithm was tested in a bending test for crack detection. As shown in Figure 2(a) and (b), a 200-cm 20-cm 24-cm slag cement-cement-bentonite (SCCB) beam was subjected to four-point bending. The utilization of cement-bentonite walls in river levee construction has been pivotal in addressing under seepage concerns, particularly in areas demanding enhanced structural integrity, such as when these walls are situated near the waterside levee toe or intersecting critical infrastructure like bridges, utilities, and roadways. Notably, SCCB material has recently garnered significant attention within the realm of levee projects due to its capability to concurrently reduce hydraulic conductivity and bolster structural strength. Nevertheless, the inherent brittleness of SCCB raises valid engineering apprehensions about its susceptibility to cracking under external loads. In light of this, our study employed SCCB as the primary material for inducing cracks while minimizing bending deformations, thus facilitating a comprehensive analysis of detecting cracks using DFOS techniques. The mix of the SCCB slurry used to cast the beam is shown below. The ratio of the total weight of slag and Portland cement over the weight of water is 0.17. The proportion of the slag in the cement (slag cement + Portland cement) is 0.8. The bentonite weighs 0.04 of the total weight of the slurry.

$$(W_{\text{slag}} + W_{\text{Portland}})/W_{\text{water}} = 0.17$$

 $W_{\text{slag}}/(W_{\text{slag}} + W_{\text{Portland}}) = 0.8$
 $W_{\text{bentonite}}/W_{\text{total}} = 0.04$

Before pouring the SCCB slurry into the wood mold of the beam, the fibers were installed in the longitudinal

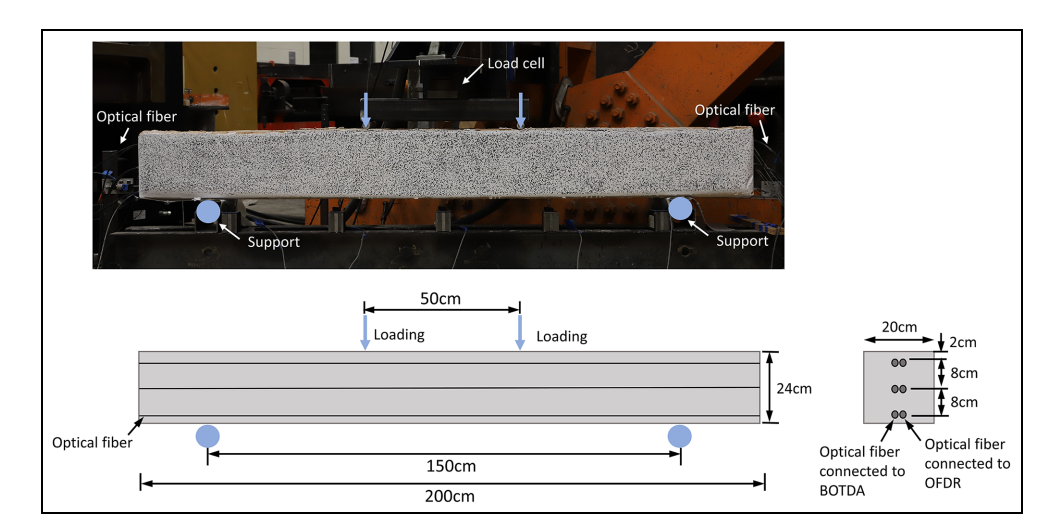


Figure 2. SCCB beam four-point bending test setup and optical fiber layout (a) photo and (b) schematic front view and cross section.

SCCB: slag cement-cement-bentonite.



Figure 3. SCCB beam and wood mold during curing. SCCB: slag cement-cement-bentonite.



Figure 4. (a) DITEST manufactured by Omnisens and (b) ODiSI6104 manufactured by LUNA Technologies.

Table 1. Specifications of Omnisens and LUNA systems.

Parameter	Omnisens DITEST	LUNA technologies ODiSI 6104
Technology	Brillouin scattering- based sensing	Rayleigh scattering- based sensing
Readout resolution	250 mm	I.3 mm
Spatial resolution Distance range	750 mm 50 km	1.3 mm 50 m
_		

direction at three different levels (2, 10, and 18 cm from the top of the beam) in the middle of the mold, as shown in Figure 2(b). Figure 3 shows the beam and the mold during the curing process. The water content of the material easily evaporates and drying cracks are generated within a short time. To prevent the water from evaporating, a plastic sheet was used to fully wrap the beam throughout the curing process.

Two optical fibers were embedded in the beam, one connected to a high spatial resolution OFDR system and the other connected to a low spatial resolution BOTDA system to measure the strain profile. Their photos and specifications are shown in Figure 4 and Table 1, respectively. The two cables were installed parallel to each other and 5 mm apart. Both were 1.3-mm-diameter single-mode tight buffer strain cables manufactured by NanZee Sensing Technology Ltd (Suzhou Industrial Park, Suzhou, China). The central frequency of the cables with no strain applied is $10.857 \, \text{Hz}$, whereas C_{ϵ} = 499.8 MHz/% and C_{T} = 0.915 MHz/°C. Because the two cables were installed parallel to each

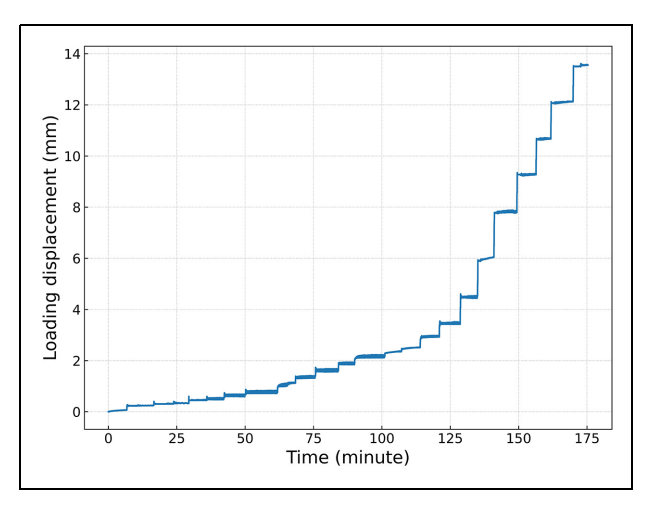


Figure 5. Loading displacement versus time curve at two loading points at 0.75 and 1.25 m from the left end of the beam.

other with a small horizontal distance in between, it was assumed that the two cables measured the same deformation, and the two DFOS techniques were employed concurrently for measurement comparison. The finely detailed strain profiles obtained through the OFDR system were utilized as the reference in this testing scenario.

The bending test was performed on the 50th day after casting the slurry. As shown in Figure 2, the spanning distance between the two loading points on top of the beam was 50 cm and the distance between the two supports at the bottom was 150 cm. The loading was conducted by a loading cell. The vertical displacements of the loading points were controlled with a precision of 0.254 mm (0.01 in). The test lasted for 175 min. During the test, the vertical displacement was gradually increased step by step from 0 to 13.97 mm, as shown in Figure 5. At each step, the loading displacement was raised to the target value and then kept constant for about 10 min to allow the BOTDA system to take measurements.

Figure 6 shows the strain profile along the fiber at the top, middle, and bottom levels before crack occurrence. The two supports and the two loading points are marked in the figure. Outside of the two supports, the strain remained constant, as expected. The fiber experienced tension at the bottom level but compression at the middle and top levels. This indicates that the bottom level is below the neutral plane whereas the middle level is above the neutral plane.

Figure 7 shows the photos of the beam under test. Two cracks were observed during the test. Crack 1 initiated at a displacement of 0.76 mm and crack 2 at 4.06 mm. Both cracks then expanded, with crack 1 expanding faster than crack 2. Finally, crack 1 crossed the beam at a displacement of 13.97 mm measured at bottom surface.

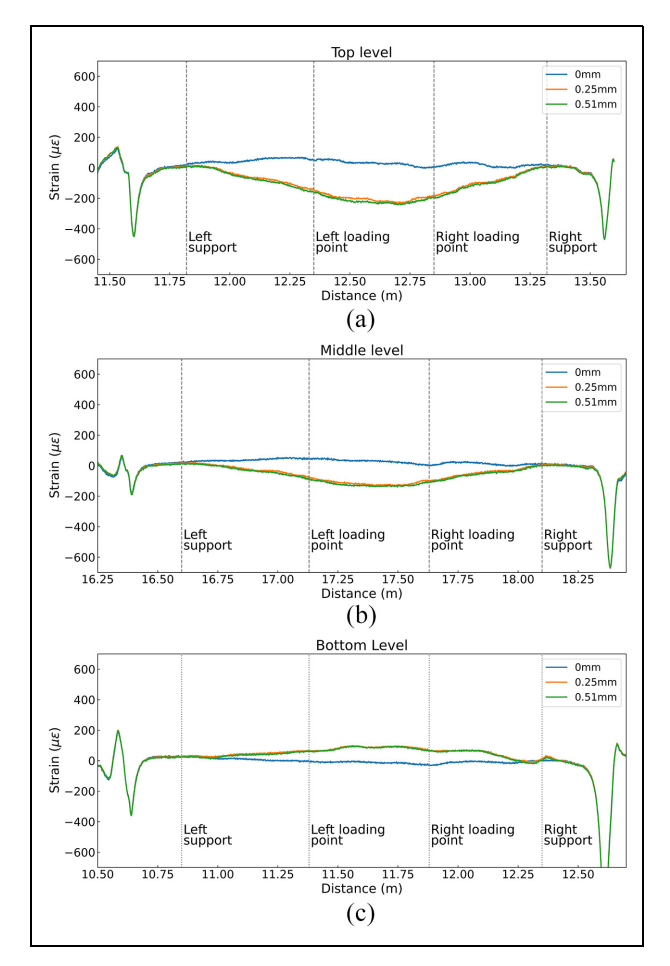


Figure 6. Strain profiles at the (a) top, (b) middle, and (3) top level before crack occurrence.

Figure 8(a), (b), and (c) show the strain profiles measured by the OFDR system along the fiber at the top, middle, and bottom levels, respectively. The strain profiles were taken with spatial resolution and readout resolution both at 1.3 mm. The figure shows that there was no crack in the beam initially. Under increasing loading, two cracks were generated during the test. Crack 1, in Figure 7, developed at a displacement of 0.76 mm, penetrated through the bottom and middle levels, then expanded and touched the top level at a displacement of 8.89 mm. Crack 2, in Figure 7, developed at a displacement of 4.06 mm and crossed the bottom, middle, and top levels at first but did not expand much at the middle and top levels during the rest of the test.

Because the BOTDA has 75 cm spatial resolution, three points on the profile can be used to cover the 200 cm beam. The BSSs at 27.5, 102.5, and 177.5 cm from the left end of the beam at the bottom, middle, and top levels are shown in Figures 9, 10, and 11. They cover ranges of [-10-65 cm], [65-140 cm], and [140-215 cm], respectively, and therefore together cover the whole beam.

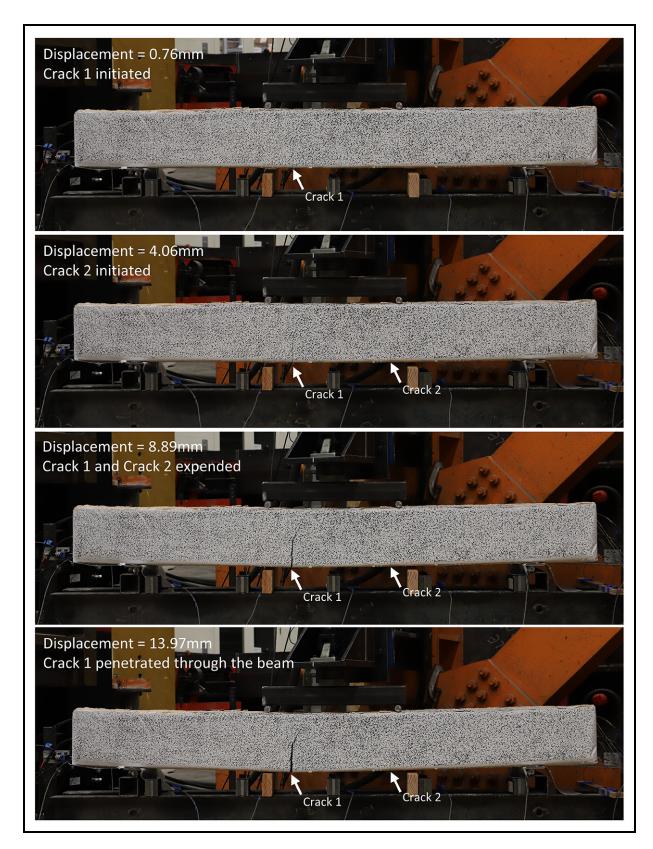


Figure 7. Crack generation stages at different loading steps. Fine spatial resolution OFDR system and low spatial resolution BOTDA system BSS measurement.

OFDR: optical frequency domain reflectometry; BOTDA: Brillouin optical time-domain analysis; BSS: Brillouin scattering spectrum.

The variation in OFDR strain profiles and the variation in BOTDA BSSs at the three levels can be divided into three stages:

Bottom level:

- Stage 1: Crack 1 appeared at displacement = 0.76 mm. In the BOTDA BSSs, crack 1 appeared within [65–140 cm] at displacement = 0.76 mm. This can be observed in the BSS at 102.5 cm, where a crack peak strain developed to be 5700 με with a secondary peak slightly developed at 11.04 GHz (Figure 9(b)).
- Stage 2: The crack opened and slippage occurred between the beam and optical fiber as the displacement increased. Slippage occurred at two different displacement levels, 1.27 and 4.06 mm, and expanded accordingly. At 1.27 mm displacement, the slippage occurred within the location ranging from 11.25 to 11.50 m. Subsequently, at 4.06 mm displacement, the second crack emerged between 11.55 and 11.85 m, and slippage also occurred, which was evident in the OFDR profile.

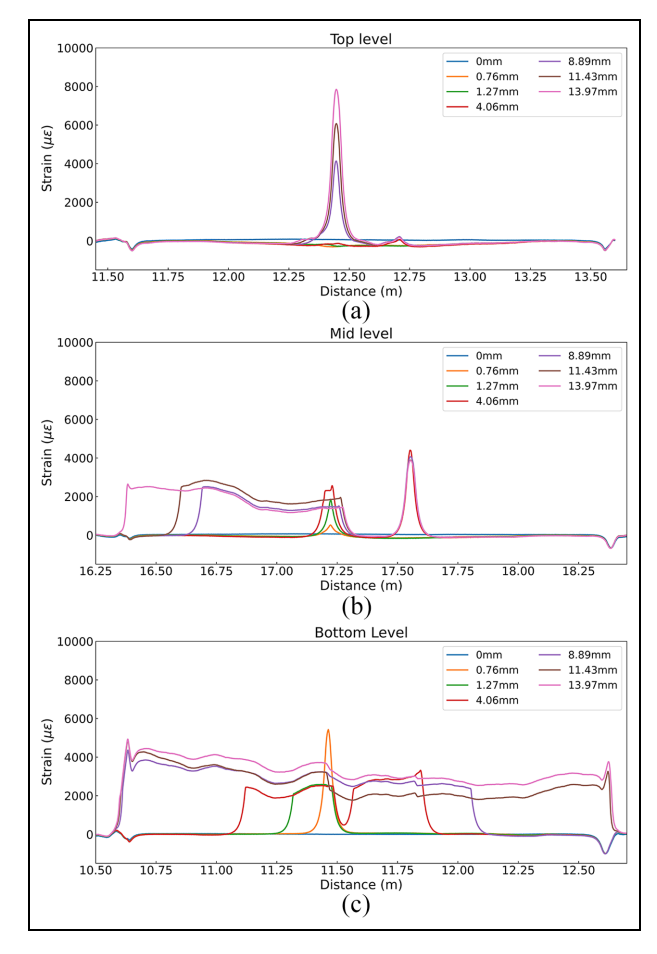


Figure 8. Strain profiles measured by the OFDR system along (a) the top, (b) middle, and (c) bottom levels at different loading steps.

OFDR: optical frequency domain reflectometry.

Regarding the BOTDA BSSs reading, there were two peaks of comparable power in the BSS as the first part of the SRW of the measurement point at 27.5 cm was below $\sim\!0~\mu\epsilon$, while the rest was below $\sim\!2,000~\mu\epsilon$ (Figure 9(a)). On the other hand, the slippage area occupied almost the entire SRW of the measurement point at 102.5 cm, and the peak in the BSS shifted directly to the larger frequency value at the 4.06 mm displacement level (Figure 9(b)).

- Stage 3: The two slippage areas merged at a displacement of 8.89 mm and expanded throughout the entire beam, leading to an approximate increase of 3000–4000 με at the whole beam in the OFDR profile. Additionally, the peaks of the BSSs in the BOTDA shifted directly to the higher frequency value (11–11.1 GHz in Figure 9) at the measurement points of 27.5, 102.5, and 177.5 cm.
- Middle level:

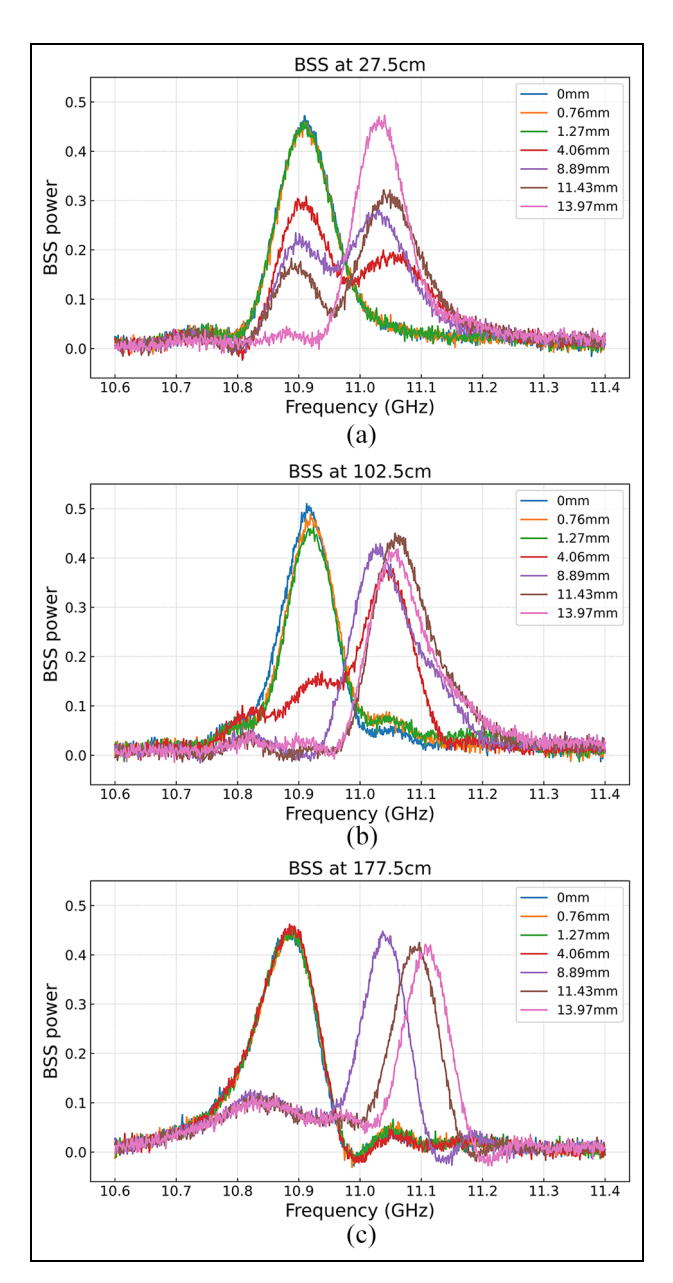


Figure 9. BSS at (a) 27.5 cm, (b) 102.5 cm, and (c) 177.5 cm from the left end of the beam along the fiber at the bottom level at different loading steps.

BSS: Brillouin scattering spectrum.

- Stage 1: In the OFDR profile, a crack (crack 1) was observed at a displacement of 0.76 mm. In BOTDA BSSs profiles, crack 1 appeared within the range of [65–140 cm] at displacement = 0.76 mm. However, the peak strain value ~150 με was not big enough to cause an obvious secondary peak in the BSS (see Figure 10(b)).
- Stage 2: OFDR profiles showed that crack 2 continued to develop, and slippage began to occur at a displacement of 4.06 mm. In the BOTDA BSSs profile,

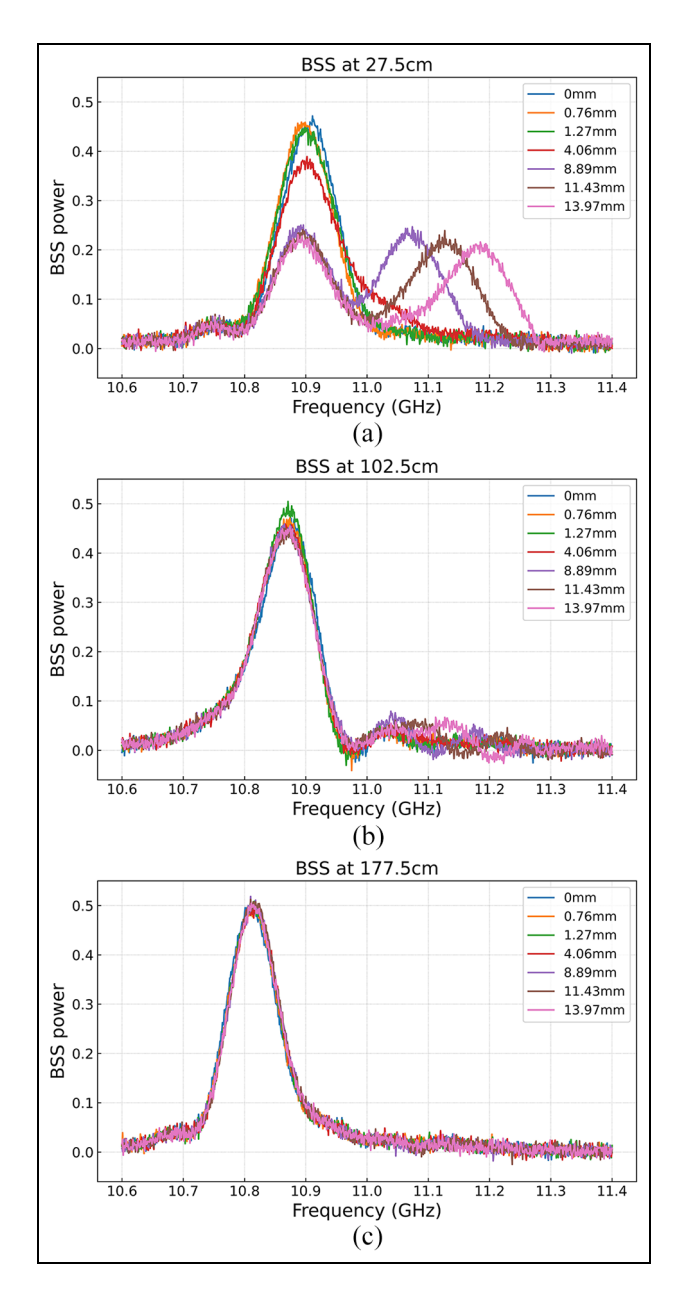


Figure 10. BSS at (a) 27.5 cm, (b) 102.5 cm, and (c) 177.5 cm from the left end of the beam along the fiber at the middle level at different loading steps.

BSS: Brillouin scattering spectrum.

the power accumulation of cracks 1 and 2 induced the appearance of a secondary peak in the BSS at 102.5 cm (see Figure 10(b)). Additionally, a slight secondary peak can be observed at 11.05 GHz in the 27.5 cm BSS (see Figure 10(a)).

- Stage 3: At a displacement of 8.89 mm, slippage began to occur and expand around crack 1 in the OFDR profile, forming a distinct pattern that emerged at 4.06 mm. The slippage area, which

experienced a large strain value of around 2000 $\mu\epsilon$, occupied approximately half of the SRW at the measurement point at 27.5 cm. As a result, the power of the two peaks in the BSS at 102.5 cm were nearly equal (see Figure 10(a)).

Top level:

- Stage 1: The OFDR profile did not show any cracks at the top level at a displacement of 1.27 mm. The BOTDA BSSs profiles at the three measurement locations each exhibited a single peak (see Figure 11).
- Stage 2: At a displacement of 4.06 mm, crack 2 was visible in the OFDR profile as a distinct feature. Despite a peak strain value of approximately 100 με.
- crack 2 did not produce a noticeable secondary peak in the BSS (see Figure 11).
- Stage 3: At a displacement of 8.89 mm, crack 1 crossed the top level and began to expand. In the BOTDA BSSs profile, crack 1 was located between 65 and 140 cm along the fiber. As crack 1 touched the top level at a displacement of 8.89 mm and expanded, a secondary peak appeared with its position shifting to the right and its power increasing in the BSSs at 102.5 cm (see Figure 11(b)).

Strain profile back-calculation from BSS data

Strain profile: BSS versus OFDR

As the crack cannot be easily observed from the BSS profile, the BSS profile was back-calculated using Equation (4). Firstly, the S_L was generated.

Because the maximum strain value the fiber can sustain is about 10,000 με, the upper bound of the estimated strain value was set to be slightly larger, at 12,000 με. During the process of crack initiation, generation, and expansion, the fiber was always under tension. The lower bound of the estimated strain value was set to be slightly smaller than 0 με, at -500 με. By assuming $\underline{a}_{min} = -500$ με, $a_{max} = 12,000$ με, and $c_i - c_{i-1} = 10$ με, C was generated as [-500 με, -490 με, ..., 11,990 με, 12,000 με] (size is 1251).

The measured BSS data G of the BSS data was set as from 10.6 to 11.4 kHz with 1 Hz steps and this gives [G(10.6 kHz), G(10.601 kHz), ..., G(11.4 kHz)] during the test; therefore, the frequency verter is $[\nu_1, \nu_2, ..., \nu_{801}] = [10.6 \text{ kHz}, 10.601 \text{ kHz}, 10.602 \text{ kHz}, ..., 11.399 \text{ kHz}, 11.4 \text{ kHz}]$. In this case, matrix S_L was generated as

$$0.55 S_{L} = \begin{bmatrix} g(10.6 \text{ kHz}, \nu_{B}(-500 \,\mu\text{e})) & g(10.6 \text{ kHz}, \nu_{B}(-490 \,\mu\text{e})) & \dots & g(10.6 \text{ kHz}, \nu_{B}(12,000 \,\mu\text{e})) \\ g(10.601 \,\text{kHz}, \nu_{B}(-500 \,\mu\text{e})) & g(10.601 \,\text{kHz}, \nu_{B}(-490 \,\mu\text{e})) & \dots & g(10.601 \,\text{kHz}, \nu_{B}(12,000 \,\mu\text{e})) \\ \dots & \dots & \dots & \dots & \dots \\ g(11.399 \,\text{kHz}, \nu_{B}(-500 \,\mu\text{e})) & g(11.399 \,\text{kHz}, \nu_{B}(-490 \,\mu\text{e})) & \dots & g(11.399 \,\text{kHz}, \nu_{B}(12,000 \,\mu\text{e})) \\ g(11.4 \,\text{kHz}, \nu_{B}(-500 \,\mu\text{e})) & g(11.4 \,\text{kHz}, \nu_{B}(-490 \,\mu\text{e})) & \dots & g(11.4 \,\text{kHz}, \nu_{B}(12,000 \,\mu\text{e})) \end{bmatrix}$$

$$(10)$$

Secondly, spatial ratios R_L were solved by NNLS from Equation (4). The solution of $R_L = [r_{c_1}, \underline{r}_{c_2}, ..., r_{c_{1251}}]$ is comprised of the spatial ratios of $C = [-500 \, \mu\epsilon, -490 \, \mu\epsilon, ..., 11,990 \, \mu\epsilon, 12,000 \, \mu\epsilon]$ from the BSSs in Figures 9, 10, and 11.

Within each SRW, that is, 75 cm in this case, around the measurement point, a single dominant crack occurs around that measurement point and strains with positive calculated spatial ratios were sorted to follow the same order as the ground truth in order to form the estimated strain profiles. The estimated strain profiles (solid lines) along the bottom, middle, and top levels are plotted against the ground truth (dotted lines) in Figures 12, 13, and 14 for comparison. As shown in these figures, the estimation and ground truth match each other.

The strain estimation errors (=estimation - truth)along the fiber at the three levels are plotted against the truth strain values in Figure 15(a). The black, blue, and red points correspond to the fiber at the top, middle, and bottom levels, respectively. Statistical analysis was conducted on these estimation errors and the results are summarized in Table 2. As shown in the table, the strain estimation accuracy is similar among the three fiber levels. The biases of the estimations are all close to 0 us. The maximum and minimum values, root mean square error (RMSE), and 95% confidence interval for the mean are similar for the three levels. In this case, the estimation errors for all levels were analyzed together to evaluate the estimation accuracy. The maximum estimation errors are -95 and $94 \mu\epsilon$. The bias of the estimation (mean of errors) is $-0.48 \mu \epsilon$. The RMSE of the estimations is 33.86 µE. Figure 15(b) shows the probability density function (pdf) of the estimation errors. Assuming this pdf follows a normal distribution, $[-0.83 \mu\epsilon]$. $-0.12 \,\mu\text{g}$ is the 95% confidence interval for the mean of the estimation error. Because the crack width is the integration of the crack strain profile, the expected crack width estimation errors at the top, middle, and bottom levels are 750 mm $\times 0.35 \mu\epsilon = 0.00026$ mm, 750 mm \times $(-2.04 \mu \epsilon) = -0.00153 \text{ mm}$, and 750 mm $\times 0.15 \mu \epsilon$ = 0.00011 mm, respectively. The accuracy evaluation of the crack width estimation in the next section confirms these numbers.

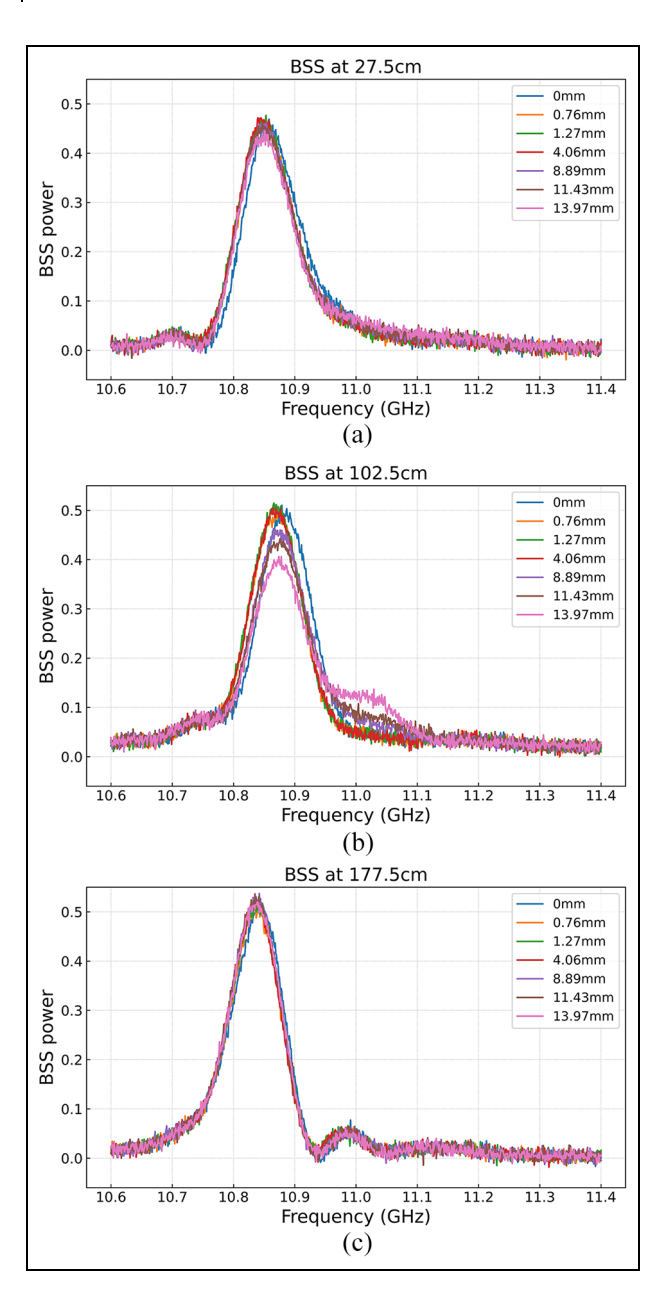


Figure 11. BSS at (a) 27.5 cm, (b) 102.5 cm, and (c) 177.5 cm from the left end of the beam along the fiber at the top level at different loading steps.

BSS: Brillouin scattering spectrum.

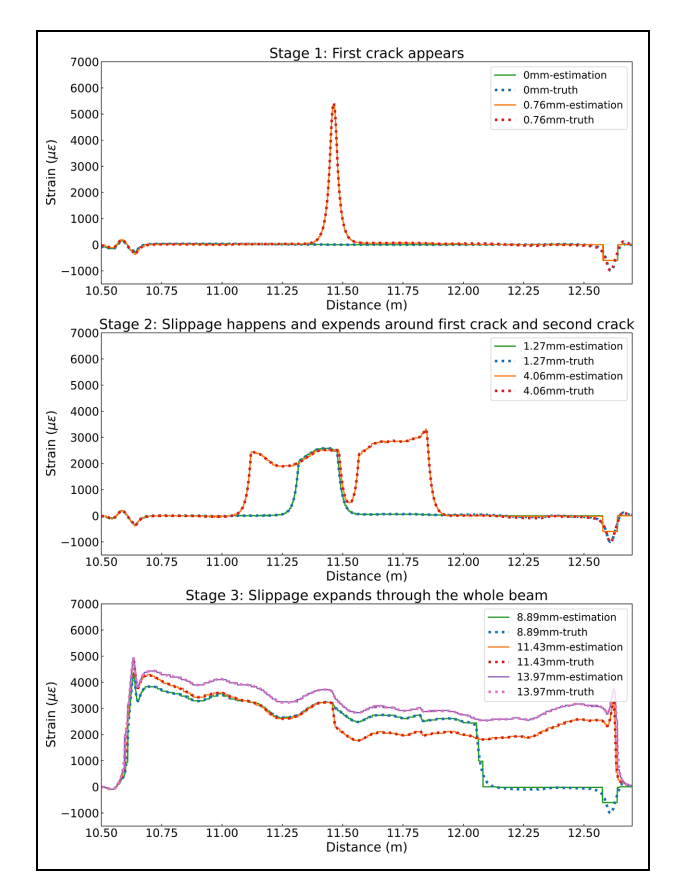


Figure 12. Comparison of the strain profile back-calculated from the BSS data and the ground truth measured by the OFDR system along the fiber at the bottom level.

OFDR: optical frequency domain reflectometry; BSS: Brillouin scattering spectrum.

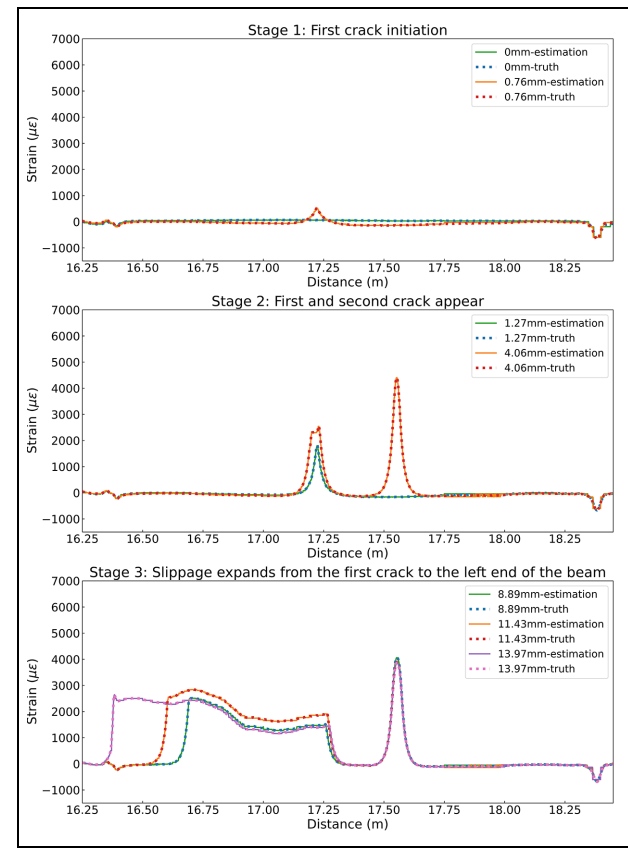


Figure 13. Comparison of the strain profile back-calculated from the BSS data and the ground truth measured by the OFDR system along the fiber at the middle level.

OFDR: optical frequency domain reflectometry; BSS: Brillouin scattering spectrum.

Table 2. Statistical analysis of strain estimation errors.

Fiber position	Top level	Middle level	Bottom level	All
Mean	0.35 με	-2.04 με	0.15 με	-0.48 με
MAE	10.85 με	10.30 με	17.06 με	I4.8I με
Max	67 με	81 με	94 με	94 με
Min	– 67 με	−82 με	–95 με	–95 με
RMSE	38.09 με	I5.80 με	41.10 με	33.86 με
R^2	0.9947	0.9996	0.9993	0.999
% CI for mean	$[-0.33~\mu ε, I.02~\mu ε]$	[$-2.33~\mu\epsilon$, $-1.74~\mu\epsilon$]	[-0.60 με,0.91 με]	[$-0.83~\mu\epsilon$, $-0.12~\mu\epsilon$]

RMSE: root mean square error; CI: confidence interval; MAE: mean absolute error.

Crack width estimation: BSS versus OFDR

The total crack displacements were calculated by taking the integral of the strain profiles in Figures 12, 13, and 14. The results for the bottom, middle, and top levels are plotted in Figure 16(a), (c), and (e), respectively. In the figures, the estimation and ground truth match each other well. Considering the OFDR measurements as the baseline, the crack width estimation

errors (=BSS estimations – OFDR measurements) for the bottom, middle, and top levels are plotted in Figure 16(b), (d), and (f), respectively. As shown in the figure, the crack width estimation errors are all within ± 0.005 mm. The means of the crack width estimation errors at the bottom, middle, and top levels are 0.00026, -0.00153, and 0.00011 mm, respectively.

In this study, due to the inherent brittleness of SCCB material, the strain resulting from bending deformation

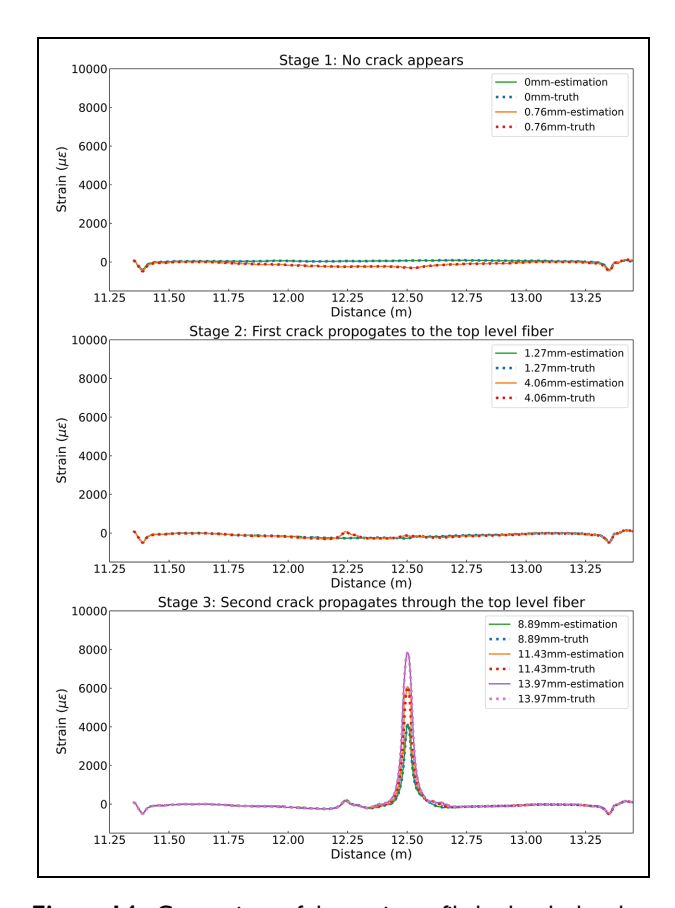


Figure 14. Comparison of the strain profile back-calculated from the BSS data and the ground truth measured by the OFDR system along the fiber at the top level.

OFDR: optical frequency domain reflectometry; BSS: Brillouin scattering spectrum.

is relatively small compared to the strain levels generated by cracks. The bending deformation, which extends across a larger spatial section, was not taken into consideration in this study. Although the BSS analysis method inherently excludes the consideration of average deformation strain within the SRW, it is important to note that this bending deformation can increase the margin of error in crack width assessment. Therefore, future research should explore this aspect further to enhance our understanding of crack behavior in other materials under different loading conditions. In this study, it is assumed that there is perfect bonding between the optical fiber and the host material, encompassing the interfaces of optical fiber-epoxy, epoxy-material, and within the optical fiber cable itself. However, it is important to acknowledge that instances of debonding between the optical fiber and the host material can potentially lead to an increase in crack width while simultaneously reducing the strain intensity in the measured data. Such occurrences may ultimately limit the precision of crack width measurements. To address this challenge, methods developed for OFDR^{11,12,14} can also be applied to the analysis of BSS-based BOTDA/R for a more accurate estimation of crack width.

It is also notable that this crack back calculation method requires the assumption that there is only one dominant crack in an SRW. If there are multiple cracks along the fiber and the distance between them is larger than the spatial resolution, the performance of this method will be the same as in the single-crack cases because each BGS will be affected by only one crack. If there are two or more cracks within an SRW, it will still be able to provide accurate estimation of crack width, since it calculates the strain values and their corresponding spatial ratios accurately. However, it cannot identify the exact locations of cracks, and thus cannot estimate strain profiles.

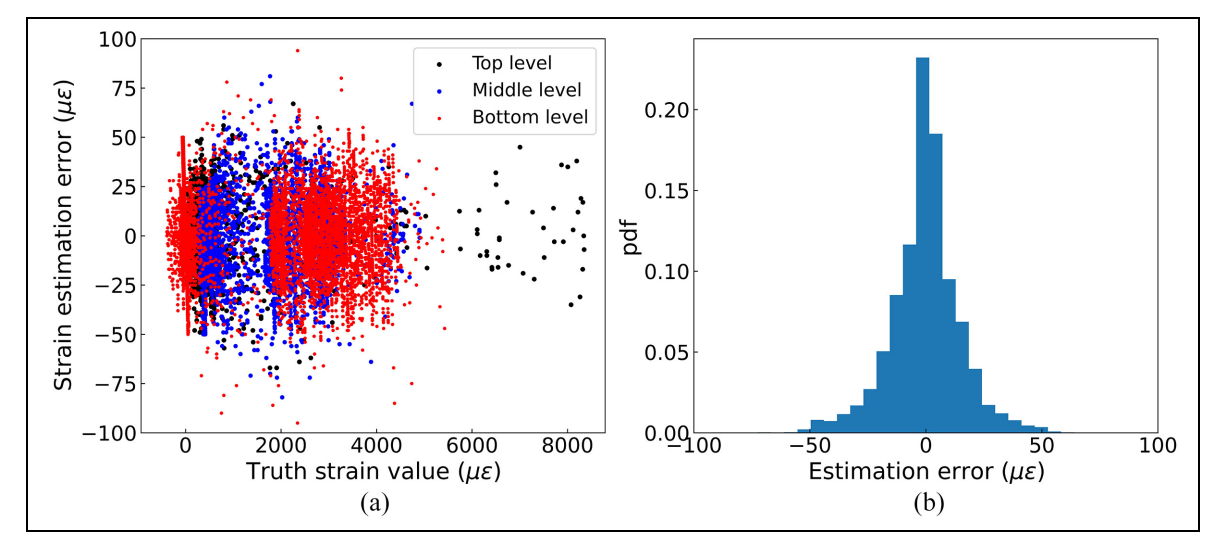


Figure 15. (a) Estimation errors versus truth strain values. (b) pdf of estimation errors.

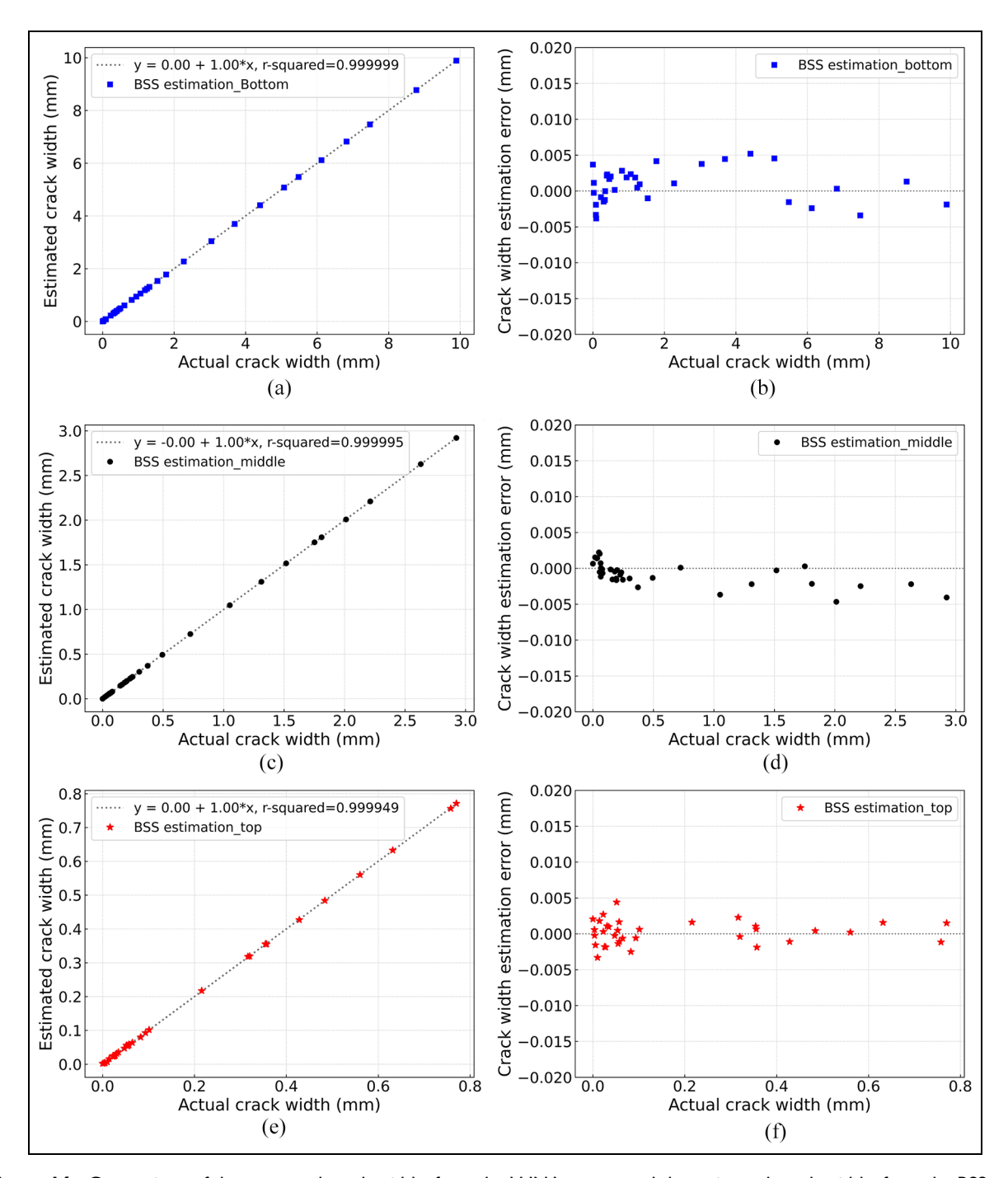


Figure 16. Comparison of the measured crack widths from the LUNA system and the estimated crack widths from the BSSs at the (a) bottom, (c) middle, and (e) top levels. Crack width estimation errors of Luna measurements and BSSs at the (b) bottom, (d) middle, and (f) top levels.

BSS: Brillouin scattering spectrum.

Conclusion

This study addresses a significant challenge in SHM by introducing a novel BSS-based crack analysis method to detect small strain events, such as cracks. This method was developed to overcome the limitation of

large spatial resolution in BOTDA/R-type DFOS systems while harnessing their long sensing distance capabilities. The methodology comprises three crucial steps: (1) estimating lower and upper bounds of strain values within a predefined spatial resolution, (2)

constructing a comprehensive strain vector encompassing all estimated values and utilizing it as a matrix within the BSS formation equation, and (3) applying the NNLS algorithm to determine spatial ratios of strain values within the generated vector. The practical significance of this innovation was demonstrated through its application to quantify cracks in a four-point bending laboratory test on an SCCB beam.

The experimental results underscore the method's utility in several key aspects. Firstly, it effectively identifies crack formation and detects fiber-material slippage during SCCB bending tests. Secondly, the method exhibits a high degree of accuracy in back-calculating strain profiles. Thirdly, it quantifies crack sizes from BSS data with exceptional precision, maintaining an error margin of only 0.005 mm. Importantly, crack generation is discerned by a subtle power increase at a high frequency within the BSS, while the pronounced secondary peak power value serves as a distinctive signature of slippage.

Furthermore, this study elucidates a discernible nonlinear mathematical relationship between the BSS and the strain profile within the spatial resolution. A significant advantage of the BSS-based crack analysis method is its capacity to linearize the problem, making it amenable to integration with deep learning models. This opens avenues for further research possibilities, as deep learning techniques can be leveraged to decompose and enhance the utility of BSS data.

However, the method's application has primarily been demonstrated within the context of SCCB beam testing, and its generalizability to other materials and structural configurations requires further exploration. Additionally, the influence of various environmental factors and potential debonding effects between the optical fiber and the host material warrants deeper investigation. Furthermore, the computational demands associated with the NNLS algorithm and the integration of deep learning techniques may present practical challenges in real-world applications. Addressing these limitations and conducting extensive validation studies across diverse settings will be pivotal in fully realizing the potential of this innovative BSS-based crack analysis method in the realm of SHM and beyond.

Declaration of conflicting interests

The author(s) declared no potential conflicts of interest with respect to the research, authorship, and/or publication of this article.

Funding

The author(s) received no financial support for the research, authorship, and/or publication of this article.

ORCID iD

Linqing Luo (D) https://orcid.org/0000-0002-7073-6588

References

- Sieko R, Zych M, Bednarski Ł, et al. Strain and crack analysis within concrete members using distributed fibre optic sensors. Struct Health Monit 2019; 18: 1510–1526.
- Feng Q, Kong Q, Huo L, et al. Crack detection and leakage monitoring on reinforced concrete pipe. Smart Mater Struct 2015; 24: 115020.
- Yao Y, Tung S and Glisic B. Crack detection and characterization techniques an overview. Struct Control Health Monit 2014; 21: 1387–1413.
- Xiao Z, Yamada K, Inoue J, et al. Fatigue cracks in longitudinal ribs of steel orthotropic deck. *Int J Fatigue* 2006; 28: 409–416.
- Ohtsu M. Acoustic emission and related non-destructive evaluation techniques in the fracture mechanics of concrete: fundamentals and applications. Duxford, UK: Woodhead Publishing, 2020.
- Dabous S, Yaghi S, Alkass S, et al. Concrete bridge deck condition assessment using IR Thermography and Ground Penetrating Radar technologies. *Autom Constr* 2017; 81: 340–354.
- Sun H, Pashoutani S and Zhu J. Nondestructive evaluation of concrete bridge decks with automated acoustic scanning system and ground penetrating radar. Sensors 2018; 18: 1955.
- 8. Deng F, Huang Y, Azarmi F, et al. Pitted corrosion detection of thermal sprayed metallic coatings using fiber Bragg grating sensors. *Coatings* 2017; 7: 35.
- Smith G, Higgins O and Sampath S. In-situ observation of strain and cracking in coated laminates by digital image correlation. Surf Coat Technol 2017; 328: 211–218.
- Xu Y, Bao Y, Chen J, et al. Surface fatigue crack identification in steel box girder of bridges by a deep fusion convolutional neural network based on consumer-grade camera images. Struct Health Monit 2019; 18: 653–674.
- Tan X, Mahjoubi S, Zou X, et al. Metaheuristic inverse analysis on interfacial mechanics of distributed fiber optic sensors undergoing interfacial debonding. *Mech* Syst Signal Process 2023; 200: 110532.
- Tan X and Bao Y. Measuring crack width using a distributed fiber optic sensor based on optical frequency domain reflectometry. *Measurement* 2021; 172: 108945.
- Tan X, Abu-Obeidah A, Bao Y, et al. Measurement and visualization of strains and cracks in CFRP posttensioned fiber reinforced concrete beams using distributed fiber optic sensors. *Autom Constr* 2021; 124: 103604.
- Zhao L, Tang F, Li H, et al. Characterization of OFDR distributed optical fiber for crack monitoring considering fiber-coating interfacial slip. Struct Health Monit 2023; 22: 180–200.
- Soga K and Luo L. Distributed fiber optics sensors for civil engineering infrastructure sensing. J Struct Integr Maint 2018; 3: 1–21 (2018)
- Bao Y, Valipour M, Meng W, et al. Distributed fiber optic sensor-enhanced detection and prediction of

- shrinkage-induced delamination of ultra-highperformance concrete overlay. *Smart Mater Struct* 2017; 26: 085009.
- 17. Leung C. Fiber optic sensors in concrete: the future? *Ndt E Int* 2001; 34: 85–94.
- 18. Wan K and Leung C. Applications of a distributed fiber optic crack sensor for concrete structures. *Sens Actuator A Phys* 2007; 135: 458–464.
- 19. Ravet F, Briffod F, Glisic B, et al. Submillimeter crack detection with Brillouin-based fiber-optic sensors. *IEEE Sens J* 2009; 9: 1391–1396.
- 20. Ou R, Luo L and Soga K. Brillouin scattering spectrum-based crack measurement using distributed fiber optic sensing. *Struct Health Monit* 2022; 21: 1345–1366.
- 21. Yu Y, Luo L, Li B, et al. Double peak-induced distance error in short-time-Fourier-transform-Brillouin optical time domain reflectometers event detection and the recovery method. *Appl Opt* 2015; 54: E196–E202.
- 22. Lawson C and Hanson R. *Solving least squares problems*. Englewood Cliffs, NJ: Prentice-Hall, 1995.
- 23. Bro R and De Jong S. A fast non-negativity-constrained least squares algorithm. *J Chemom* 1997; 11: 393–401.